





Cite this: *RSC Adv.*, 2025, 15, 24905

# Sub-10 nm Yb<sup>3+</sup>/Er<sup>3+</sup>-doped NaYF<sub>4</sub> core-shell upconversion nanoparticles: precise size control and enhanced luminescence†

Umme Farva,  Young Gwon Jung  and Kang Taek Lee \*

Upconversion nanoparticles (UCNPs) exhibit unique photophysical properties that are ideal for bioimaging, photovoltaics, and optoelectronics. This study systematically investigates how synthesis temperature (305 °C vs. 320 °C) and reaction time (20–30 min) influence the structural and optical properties of Yb<sup>3+</sup>/Er<sup>3+</sup>-doped NaYF<sub>4</sub> core-shell UCNPs. By employing an optimized precursor dissolution protocol, we achieved precise control over nanoparticle size, crystallinity, and upconversion luminescence (UCL). High-resolution transmission electron microscopy (HR-TEM), X-ray diffraction (XRD), luminescence spectroscopy, and power-dependent emission analyses revealed that both temperature and reaction time significantly regulate particle growth and UCL properties. Pure hexagonal β-NaYF<sub>4</sub> structures with enhanced crystallinity were confirmed by sharper, more intense XRD peaks under optimized conditions. Morphological transitions from small spherical nanoparticles (9.75 nm) to larger anisotropic structures (13.3–19.1 nm) were accompanied by tunable emission and controllable red-to-green (R/G) emission ratios. Power-dependent analyses further confirmed the effectiveness of two-photon upconversion mechanisms, providing insights into the underlying energy transfer dynamics involved. Remarkably, compared to the conventional method, the optimized protocol reduced reaction duration by 50%, consistently yielding highly uniform and crystalline UCNPs with significantly improved upconversion efficiency. These findings underscore the critical role of synthesis temperature and reaction duration in precisely tailoring UCNP properties for advanced bioimaging and photonic applications.

Received 7th April 2025  
Accepted 27th June 2025

DOI: 10.1039/d5ra02389k

rsc.li/rsc-advances

## 1 Introduction

Upconversion nanoparticles (UCNPs) are a transformative class of optical nanomaterials capable of converting low-energy photons into higher-energy emissions through non-linear optical processes.<sup>1–6</sup> These unique properties arise from energy transfer between sensitizer (e.g., Yb<sup>3+</sup>) and activator (e.g., Er<sup>3+</sup>, Tm<sup>3+</sup>) ions embedded in host matrices such as β-NaYF<sub>4</sub>.<sup>7</sup> Known for their high chemical stability, low phonon energy, and transparency in the near-infrared (NIR) region,<sup>8,9</sup> β-NaYF<sub>4</sub>-based UCNPs exhibit emissions ranging from UV to NIR. This versatility makes them suitable for applications in bioimaging,<sup>10,11</sup> theranostics, anti-counterfeiting,<sup>12</sup> microlasers,<sup>13</sup> sensors,<sup>14</sup> and advanced photonic devices.<sup>15,16</sup> Their deep-tissue penetration, high photostability, and resistance to photobleaching further distinguish them from traditional fluorescence probes.

Despite their potential, UCNPs face significant challenges in biomedical,<sup>17,18</sup> and photonic applications. Issues such as large

particle size (>10 nm), low luminescence quantum yields (UCQYs), and surface quenching<sup>10,19–21</sup> hinder their widespread adoption. Precise control over emission properties, particularly the red-to-green (R/G) ratio, is critical for optimizing performance in deep-tissue imaging and energy-efficient photonics. Recent advancements, including dopant tuning, host lattice modifications, and core-shell architectures, have improved luminescence efficiency by mitigate surface quenching. However, achieving precise control over core-shell structure, particle size, and emission characteristics demands a deeper understanding of synthesis parameters.<sup>22,23</sup>

UCNP synthesis typically involves high-temperature co-precipitation or thermal decomposition methods, employing lanthanide precursors dissolved in organic solvents like oleic acid (OA), oleylamine (OM), and 1-octadecene (ODE).<sup>23,24</sup>

These solvents function simultaneously as reaction media and surfactants, influencing particle crystallinity, size, and morphology. Fig. 1 illustrates a schematic overview of the synthesis protocol, emphasizing key parameters that determine the final characteristics of UCNPs. Even minor adjustments in synthesis conditions and precursor selection can significantly alter the size, shape, and emission properties of UCNPs (Tables S1 and S2†). Parameters such as dopant ratios and solvent composition have been extensively studied.<sup>4,25</sup> For instance,

Department of Chemistry, Gwangju Institute of Science and Technology (GIST), Gwangju 61005, Republic of Korea. E-mail: ktleee@gist.ac.kr

† Electronic supplementary information (ESI) available. See DOI: <https://doi.org/10.1039/d5ra02389k>



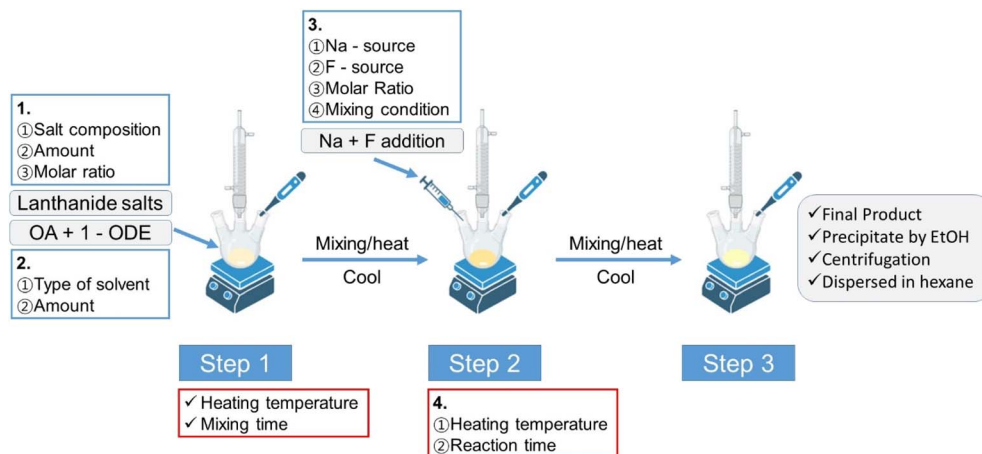


Fig. 1 Schematic representation of the synthesis protocol for NaYF<sub>4</sub>:Yb, Er core UCNP: Step 1: Dissolution of lanthanide salts to form a homogeneous solution. Step 2: The addition of precursors to facilitate nanoparticle formation. Step 3: Synthesis under controlled conditions, followed by purification to isolate the desired UCNP.

higher OA content often results in rod-shaped UCNP,<sup>3,23</sup> whereas sodium-to-fluoride mixing conditions influence particle size,<sup>26</sup> and the Y<sup>3+</sup>:F<sup>-</sup> ratio critically determines the crystalline phase.<sup>27</sup> Although UCNP synthesis has been thoroughly investigated,<sup>4,23,26,28,29</sup> with precise control, demonstrated over core-shell configurations,<sup>30–32</sup> the effects of reaction temperature and time remain less explored. While particle size typically increases with higher reaction temperature and prolonged duration,<sup>3,23</sup> detailed studies on particle growth mechanisms and associated luminescent behaviors are still necessary to fully optimize UCNP performance for practical applications. Moreover, systematic control over the red-to-green (R/G) emission ratio during synthesis is largely unexamined. Variations in ligand-to-metal ratios or solvent composition during the initial dissolution phase influence anisotropic growth and luminescence efficiency. Additionally, recent advances in surface passivation, such as ultra-thin inert shells, have shown the potential to enhance UCL by minimizing non-radiative decay pathways.

To address these gaps, we systematically investigated how synthesis temperature and time influence the structural and optical properties of Yb<sup>3+</sup>/Er<sup>3+</sup>-doped  $\beta$ -NaYF<sub>4</sub> core-shell UCNP. Initial optimization studies were briefly conducted to select suitable precursor dissolution conditions, details of which are provided in the ESI†. The optimized synthesis protocol was then employed in detailed temperature-dependent (305 °C vs. 320 °C) and time-dependent (20–30 min) investigations. A detailed summary of all synthesis conditions (including temperatures and reaction times for core and core-shell UCNP) is provided in Table S3 in the ESI†. Using HR-TEM, luminescence spectroscopy, and power-dependent analyses, we examined the impacts of reaction temperature, time, and protective shell formation on UCNP morphology and emission characteristics. Optimizing these synthesis conditions allowed precise control over nanoparticle size and fine-tuning of the R/G emission ratio. Furthermore, this approach reduced the reaction time by up to 50%, producing uniform UCNP with

significantly enhanced upconversion efficiency. This study thus advances the fundamental understanding of UCNP synthesis and provides a scalable strategy for designing next-generation nanoparticles tailored specifically for bioimaging, photonics, and energy applications.

## 2 Results and discussion

The dissolution of precursors plays an important role in synthesizing nanoparticles, because it significantly influences nucleation kinetics, particle uniformity, and dopant distribution.<sup>25,33</sup> Inadequate dissolution can lead to uneven nucleation and uncontrolled particle growth, negatively affecting crystallinity and optical properties. To avoid these issues, precursor dissolution conditions were initially screened to determine an optimal synthesis protocol (details provided in ESI†). The optimal condition identified from this preliminary study was then employed to systematically examine the effects of synthesis temperature and reaction time on nanoparticle growth and luminescence properties.

### 2.1. Temperature-dependent core and core-shell upconversion nanoparticles

Core NaYF<sub>4</sub>:Yb<sup>3+</sup> (0.2 mol%) Er<sup>3+</sup> (0.02 mol%) UCNP were synthesized at two growth temperatures: 305 °C and 320 °C. A modified thermal decomposition method, adapted from previously published reports,<sup>4,27</sup> was employed. The doping concentrations of Yb<sup>3+</sup> (20%) and Er<sup>3+</sup> (2%) were selected based on previously established optimal ratios that effectively balance efficient energy absorption by Yb<sup>3+</sup> ions and minimize concentration-quenching effects associated with Er<sup>3+</sup> ions.<sup>3,25,27,28,34</sup> To reduce surface quenching, an inert NaYF<sub>4</sub> shell was applied to the core UCNP.<sup>35</sup> TEM images (Fig. 2a and b) display highly uniform, crystalline spherical particles in both core and core-shell UCNP. The size distribution histograms (Fig. 2c) confirm a narrow particle size distribution, highlighting the uniformity of the synthesis process. The core



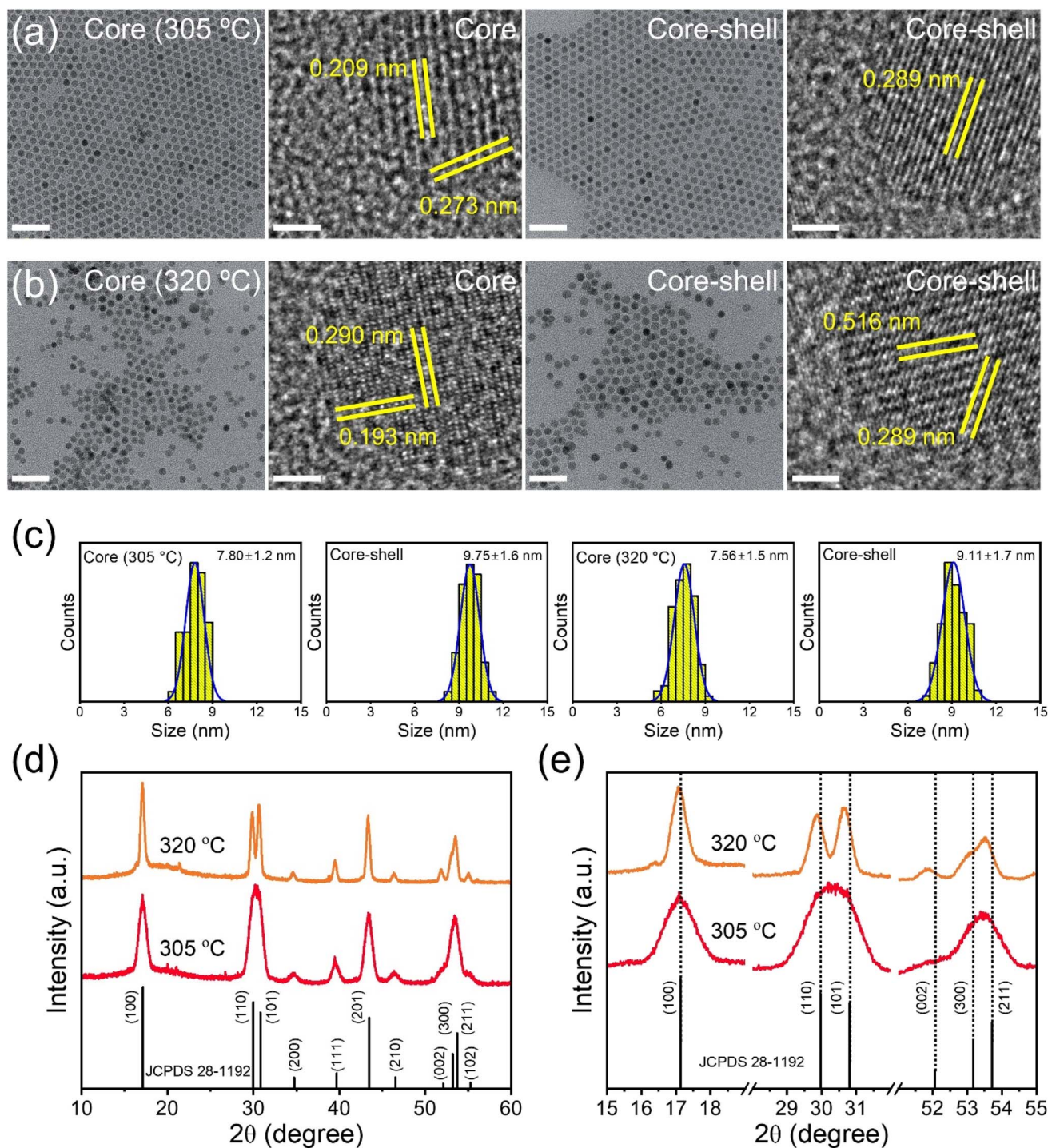


Fig. 2 (a) and (b) TEM images and HR-TEM images of core and core-shell UCNPs synthesized at 305 °C and 320 °C (scale bars: 50 nm and 5 nm, respectively). (c) Size distribution histograms of the cores at 305 °C and 320 °C, along with those of their core-shell UCNPs. (d) XRD patterns (10–60°) of core-shell UCNPs. (e) Magnified diffraction patterns at 15–19°, 28–32°, and 51–55°.

UCNPs synthesized at 305 °C, and their core-shell counterparts measured 7.80 nm and 9.75 nm, respectively, while the core UCNPs synthesized at 320 °C exhibited a slightly smaller size of 7.56 nm,<sup>36</sup> with their core-shell size at 9.11 nm.<sup>23</sup>

However, the size of UCNPs increased ( $\sim 3$  nm) as the temperature rose from 310 to 320 °C during synthesis with

sodium oleate.<sup>27</sup> HR-TEM images (Fig. 2a and b) reveal distinct lattice fringes, confirming the crystallinity of core and core-shell UCNPs. The core UCNPs exhibit fringes corresponding to the (200) and (201) planes (Fig. S1†), with  $d$ -spacings of 0.273 nm and 0.209 nm, respectively.<sup>37</sup> In contrast, the core-shell UCNPs show fringes corresponding to the (101) plane,



with a *d*-spacing value of 0.289 nm. The UCNPs synthesized at 320 °C exhibited additional lattice spacing of 0.290 nm and 0.193 nm for the (101) and (210) planes in the core and 0.516 nm and 0.289 nm for the (100) and (101) planes in the core-shell structure, indicating well-defined crystallinity in the hexagonal  $\beta$ -phase of NaYF<sub>4</sub> structure.<sup>1,4,26–28</sup>

XRD patterns (Fig. 2d) confirm the crystalline nature of the core-shell UCNPs synthesized at 305 °C and 320 °C. The observed diffraction peaks correspond to the hexagonal phase of NaYF<sub>4</sub>, indexed by the JCPDS card (28-1192),<sup>1,36,38,39</sup> validating phase purity. As shown in Fig. S2,† the core UCNPs synthesized at 280 °C exhibit diffraction peaks corresponding to the cubic  $\alpha$ -phase, while those synthesized at 320 °C show sharp peaks matching the hexagonal  $\beta$ -NaYF<sub>4</sub> structure, confirming that elevated temperatures above 300 °C are required to drive the cubic-to-hexagonal phase transformation.<sup>24,25</sup> Fig. S3† further confirms that all core UCNP samples synthesized at 320 °C exhibit pure hexagonal  $\beta$ -phase diffraction patterns. The progressive sharpening of peaks with increasing reaction time indicates enhanced crystallinity and reduced structural disorder, consistent with Ostwald ripening and thermally driven recrystallization. A slight shift in peak positions (Fig. 2e) indicates thermal effects on lattice parameters, while the sharper peaks in the 320 °C sample confirm enhanced crystallinity compared to the 305 °C sample. The observed improvement in crystallinity at higher temperature is attributed to Ostwald ripening, dissolution–recrystallization, and secondary nucleation, collectively reducing internal defects and stabilizing nanoparticles growth. Ostwald ripening involves the dissolution of smaller particles and redeposition onto larger nuclei, a process particularly enhanced at elevated temperatures due to increased thermal energy. This increased thermal energy strengthens the driving force for crystallization, favoring the formation of well-ordered nanoparticles. Additionally, thermal energy facilitates lattice strain relaxation, resulting in nanoparticles with reduced structural disorder and enhanced crystallinity.<sup>25,36,40</sup>

The UCL spectra (Fig. 3a) for core and core-shell UCNPs synthesized at both temperatures revealed sharp, intense peaks at 525 and 540 nm (green emission) and relatively high-intensity peaks at 654 nm (red emission). These emissions correspond to the transitions of Er<sup>3+</sup> ions ( $^2\text{H}_{11/2} \rightarrow ^4\text{I}_{15/2}$ ,  $^4\text{S}_{3/2} \rightarrow ^4\text{I}_{15/2}$ , and  $^4\text{F}_{9/2} \rightarrow ^4\text{I}_{15/2}$ ), which are highly efficient for photon upconversion.<sup>41</sup> The UCL intensity is significantly influenced by the surface quenching effect.<sup>22,42</sup> The core-shell UCNPs enhanced threefold and two-and-a-half-fold in UCL intensity compared to the core UCNPs, confirming that the NaYF<sub>4</sub> acts as an inert isolation layer, consistent with past studies.<sup>2,28,43–45</sup> This enhancement confirms the role of the shell in suppressing surface quenching. The core UCNPs at 320 °C exhibited stronger UCL (Fig. S4†) than those at 305 °C, attributed to improved crystallinity at higher growth temperatures.<sup>26,39</sup>

To further investigate the role of shell thickness in luminescence enhancement, we systematically varied the shell thickness from  $\sim 7$  nm to 10 nm (Fig. S5†). A clear increase in upconversion emission intensity was observed with increasing shell thickness, attributed to the progressive suppression of

surface quenching. Notably, the 28 nm core-shell UCNPs (with a 10.2 nm shell) exhibited the highest emission, showing more than a fourfold enhancement compared to the core-only sample. These findings align well with previous reports and highlight the importance of shell engineering in optimizing UCL efficiency.<sup>5,34</sup>

The R/G ratio (Fig. S6†) was higher in core UCNPs than in core-shell UCNPs at both temperatures, indicating stronger red and weaker green emissions for the core particles. The shell effectively reduced surface quenching, particularly in red emissions, which are more susceptible to quenching due to their proximity to the band edge of the host. The shell also facilitated energy transfer,<sup>35</sup> enhancing green emissions *via* a multi-photon process, resulting in an decreased R/G ratio in the core-shell UCNPs. As shown in Table S4,† the R/G emission ratio for core UCNPs decreases with increasing synthesis temperature (from 1.40 at 305 °C to 1.28 at 320 °C), suggesting a stronger quenching effect on the red-emitting  $^4\text{F}_{9/2}$  level. This is attributed to the smaller energy gap of the  $^4\text{F}_{9/2} \rightarrow ^4\text{I}_{15/2}$  transition, which is more susceptible to non-radiative multi-phonon relaxation at elevated temperatures. In contrast, green-emitting levels ( $^2\text{H}_{11/2}$  and  $^4\text{S}_{3/2}$ ) are relatively less affected. For core-shell UCNPs, a slight increase in the R/G ratio from 1.15 to 1.20 suggests that the inert shell helps mitigate thermal quenching effects, preserving red emission.

For power-dependent measurement, the laser power was varied between 4.14 W cm<sup>−2</sup> and 19.67 W cm<sup>−2</sup>. The relationship between UC emission intensity (*I*) and excitation pump power (*P*) for upconversion processes is described by the power-law equation:<sup>32,46</sup>

$$I_{\text{up}} \propto P^n \quad (1)$$

(where *I*<sub>up</sub> represents the UC emission intensity, *P* is the excitation pump power, and *n* indicates the number of photons involved in the UC mechanism). The value of '*n*' can be determined from the slope of the  $\ln(I)$  versus  $\ln(P)$  plot using linear fitting.<sup>39,45</sup> The red and green emissions of Er<sup>3+</sup> ions typically require approximately two photons to complete the energy transfer process.<sup>46</sup> This indicates that both emissions follow a two-photon process in the non-saturated state. Fig. 3b and S7† display the emission spectra at varying laser powers during a single trapping event, demonstrating that the luminescent intensity rises in proportion to the laser power.

The logarithmic plots (Fig. 3c) of intensity (Log *I*) at 540 nm and 654 nm versus power density (Log *P*) revealed distinct power-law behaviors. At 305 °C, the slopes for green and red emissions were 1.79 and 2.02, respectively, confirming efficient two-photon upconversion. At 320 °C, the slopes decreased to 1.58 (green) and 1.86 (red), indicating slight reductions in efficiency due to smaller particle sizes.

The R/G ratio as a function of pump power is shown in Fig. 3d. At both growth temperatures, 305 °C and 320 °C, the R/G emission ratio increases nonlinearly with pump power, reflecting the energy transfer upconversion dynamics between Er<sup>3+</sup> ions. The R/G ratio grows gradually at lower pump powers, but at higher powers, the curve saturates, indicating a limit to



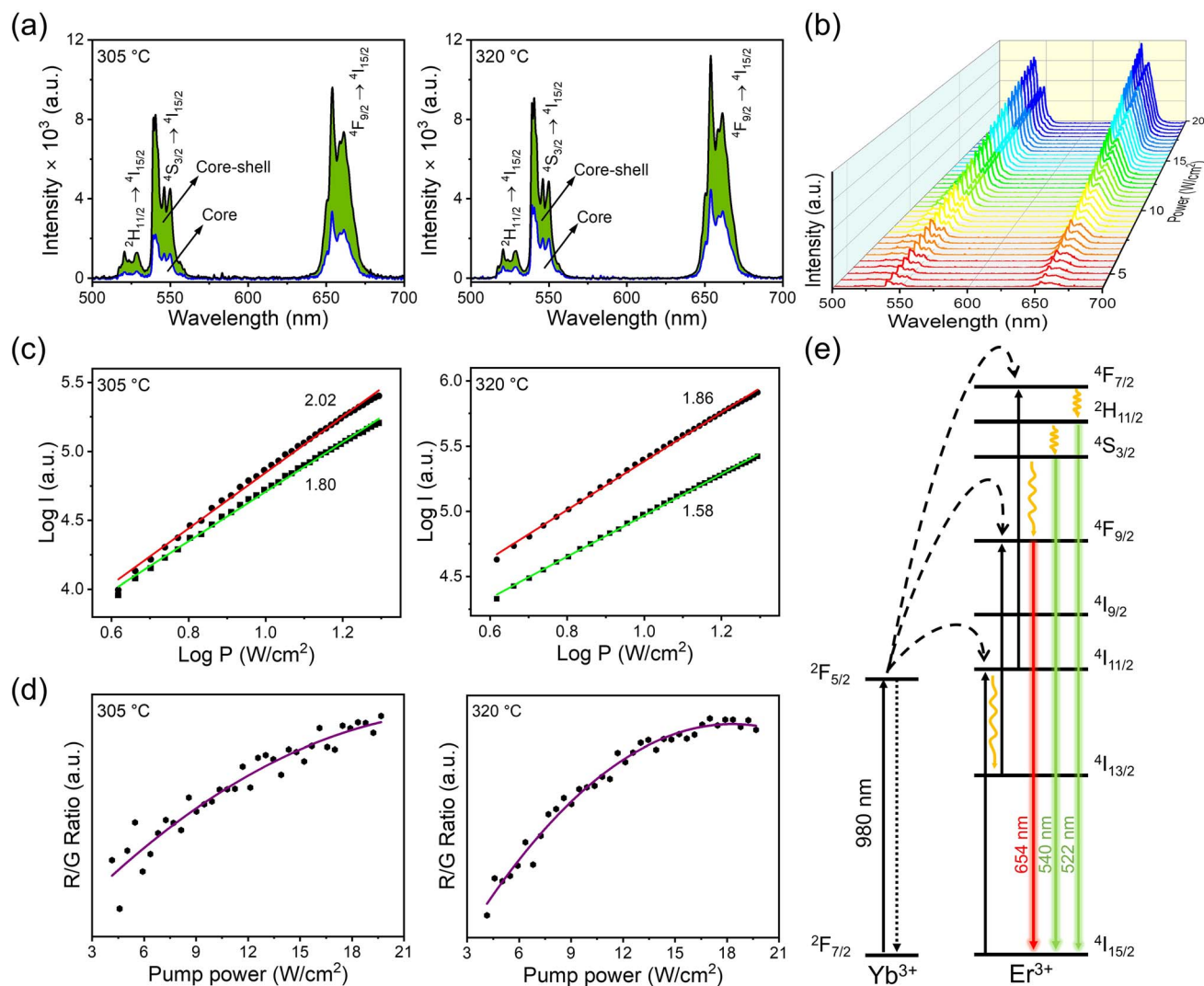


Fig. 3 (a) Emission spectra of core and core-shell UCNPs synthesized at 305 °C and 320 °C, excited by a 980 nm laser. (b) Variation in upconversion emission spectra for NaYF<sub>4</sub>:Yb/Er@NaYF<sub>4</sub> UCNPs synthesized at 305 °C as the laser power increases from 4.14 W cm<sup>-2</sup> to 19.67 W cm<sup>-2</sup>. (c) Log I vs. Log P for green and red emissions in core-shell UCNPs. (d) R/G ratio vs. pump power. (e) Energy level diagram illustrating the UC process in Yb<sup>3+</sup>/Er<sup>3+</sup> co-doped NaYF<sub>4</sub> UCNPs.

further increases in the R/G ratio. The UCNPs synthesized at 320 °C exhibit a steeper R/G ratio increase and earlier saturation compared to the 305 °C sample, indicating enhanced energy transfer efficiency and reduced non-radiative losses. In contrast, the 305 °C sample displays a more gradual increase in the R/G ratio, suggesting slower excitation dynamics. It is important to note that previous reports indicate typical UCQYs in the range of 0.005–0.01% for similarly sized (~10 nm) Yb<sup>3+</sup>/Er<sup>3+</sup>-doped NaYF<sub>4</sub> UCNPs.<sup>27,47</sup> Core-shell architectures are known to significantly enhance these values (up to approximately 0.3%), aligning well with our observed improvements in luminescence intensity achieved through optimized synthesis conditions.

The energy transfer process from Yb<sup>3+</sup> to Er<sup>3+</sup> ions occurs *via* a multi-phonon mechanism, allowing efficient NIR photon absorption by Yb<sup>3+</sup> ions and subsequent non-radiative energy transfer to Er<sup>3+</sup> ions. This mechanism enhances excitation efficiency, resulting in green (520–560 nm) and red (654 nm)

luminescence. In this process, Yb<sup>3+</sup> ions in the  $2F_{7/2}$  state absorb NIR photons and transition to the  $2F_{5/2}$  state, non-radiatively transferring energy to Er<sup>3+</sup> ions. Er<sup>3+</sup> ions then undergo multiple energy level transitions through a multi-step energy transfer upconversion (ETU) process, involving states such as  $4I_{11/2}$ ,  $4F_{9/2}$ , and  $4S_{3/2}$ , leading to visible emissions. The excitation and relaxation pathways of Er<sup>3+</sup> ions are completed in two steps. Fig. 3e illustrates the initial excitation of Er from  $4I_{15/2}$  (ground state) to  $4I_{11/2}$ . Yb<sup>3+</sup> further excites Er<sup>3+</sup> to  $4F_{9/2}$ , while Er<sup>3+</sup> non-radiatively relaxes from  $4F_{7/2}$  to  $2H_{11/2}$ ,  $4S_{3/2}$ , and  $4F_{9/2}$ , resulting in visible emission. Additionally, it is noted that the enhancement of red emission is primarily due to the efficient cross-relaxation processes in the Er<sup>3+</sup> ion ( $4I_{11/2} + 4F_{7/2} \rightarrow 4F_{9/2}$ ).<sup>39</sup>

The CIE (Commission Internationale de l'Eclairage) chromaticity diagram (Fig. S8†) illustrates the emission properties of UCNPs. Core-shell UCNPs synthesized at 305 °C exhibited chromaticity coordinates favoring green emission (~540 nm),

while UCNPs synthesized at 320 °C shifted toward yellow (~560 nm), confirming an increased population of red-emitting level ( $^4F_{9/2}$ ) with rising temperature. The higher synthesis temperatures modified the crystal field around  $Er^{3+}$  ions,<sup>48</sup> promoting non-radiative pathways that enhanced red emissions.

The unexpectedly small particle size obtained at elevated synthesis temperatures can be rationalized by considering Ostwald ripening dynamics. As described by van Westen and Groot,<sup>40</sup> temperature variations strongly influence particle dissolution and subsequent growth. According to their derivation, the change in nanoparticle radius  $r$  over time  $t$  follows:

$$\frac{dr}{dt} = D \frac{V_m \gamma}{RT r^2} \left( \frac{C}{C_\infty} - 1 \right) \quad (2)$$

Here,  $D$  is the diffusion coefficient,  $V_m$  is the molar volume,  $\gamma$  is the interfacial tension,  $R$  is the universal gas constant,  $T$  is absolute temperature,  $C$  is the solute concentration at the particle surface, and  $C_\infty$  is the bulk solute concentration. This relationship indicates that elevated synthesis temperatures can enhance particle dissolution rates, effectively stabilizing smaller nanoparticles by favoring the dissolution of larger, less stable nuclei.

## 2.2. Time-dependent variations in core and core-shell UCNPs

Fig. 4a and S9† present TEM images of core and core-shell UCNPs synthesized with reaction durations of 20, 25, and 30 min. No aggregation was observed. The particle-size distribution histogram in Fig. 4b indicates a narrow size distribution. UCNPs synthesized at 20 min were smaller (core: 11.4 nm; core-shell: width 13.3 nm, length 19.1 nm), suggesting anisotropic particle growth. With increased synthesis time, particle size gradually increased, with core UCNPs reaching 14.3 nm at 25 min and exhibiting a significantly larger size of 42.2 nm at 30 min. Correspondingly, core-shell UCNPs also increased in size up to 46.8 nm, adopting larger polyhedral shapes, confirming progressive structural evolution over time. HR-TEM analysis (Fig. S10†) revealed clear and well-defined lattice fringes with a spacing of 0.289 nm (101) crystal plane, confirming the hexagonal  $\beta$ -phase  $NaYF_4$  structure.<sup>4,23,32,49</sup> Additional HR-TEM (Fig. 4a) of 30 min UCNPs showed distinct lattice fringes with the spacing of 0.513 nm, 0.288 nm, 0.259, and 0.193 nm, indicative of a highly crystalline structure. The corresponding SAED pattern identifies (100), (101), (200), and (210) planes, confirming the hexagonal phase.<sup>23,32,44</sup>

XRD analysis (Fig. 4c) confirmed  $\beta$ -phase  $NaYF_4$  (JCPDS 28-1192)<sup>1,38,39</sup> and demonstrated that increased synthesis duration improved crystallinity. Specifically, diffraction patterns showed sharper peaks with increased reaction time (from 20 min to 30 min), reflecting greater crystallite size, enhanced atomic ordering, and reduced lattice defects.<sup>27,28</sup> At 20 min, broader diffraction peaks indicated smaller nanoparticles and structural defects, while 30 min synthesis provided highly crystalline and uniform nanoparticles.

The absence of significant peak shifts confirmed minimal strain variations. These results demonstrate that prolonged synthesis enhances structural integrity, yielding well-crystallized, phase-pure UCNPs with improved optical and physical properties, corroborated by TEM analysis.

Fig. 4d illustrates the time-dependent growth of UCNPs by plotting particle size against synthesis duration (20 min, 25 min, and 30 min). Initially, extending the reaction time from 20 min to 25 min led to a moderate particle-size increase (~25.4%). However, prolonging the synthesis duration by an additional 5 min (25 min to 30 min) resulted in a significant particle-size increment (~195.4%). This drastic growth acceleration clearly reflects Ostwald ripening dynamics, wherein smaller nanoparticles preferentially dissolve, releasing ions that subsequently redeposit onto larger nanoparticles, thus driving significant particle enlargement and morphological evolution. This mechanism aligns closely with previous studies by Rinkel *et al.*, who reported similar particle-growth patterns associated with the transformation from cubic ( $\alpha$ -phase) to hexagonal ( $\beta$ -phase)  $NaYF_4$  structures over prolonged synthesis times.<sup>32</sup> This further supports the crucial influence of reaction time in determining the final nanoparticle size and morphology.

The UCL spectra of time-dependent core and core-shell UCNPs (Fig. 5a) showed sharp emission peaks at 520 nm, 540 nm, and 654 nm, corresponding to the  $Er^{3+}$  transitions  $^2H_{11/2} \rightarrow ^4I_{15/2}$ ,  $^4S_{3/2} \rightarrow ^4I_{15/2}$ , and  $^4F_{9/2} \rightarrow ^4I_{15/2}$ , respectively. Core-shell structures had stronger UCL due to reduced surface quenching and improved energy transfer,<sup>45</sup> confirming an efficient upconversion process in all samples. Variations in shape and configuration affect the luminescence properties of the nanoparticles by altering surface area, shell thickness, and overall geometry.<sup>23</sup> The 30 min core also showed the highest intensity due to increased crystallinity from extended growth time. Fig. 5b presents the normalized luminescence spectra (at 654 nm) of core-shell UCNPs, revealing notable spectral changes as green emission intensity decreases as particle size increases.

Fig. 5c presents the red-to-green (R/G) emission intensity ratios (Table S4†). Time-dependent, the core's R/G ratio initially decreases from 20 min to 25 min but increases sharply at 30 min. In contrast, the core-shell ratio gradually increases throughout synthesis, suggesting that the shell stabilizes the environment around the  $Er^{3+}$  ions, enhancing red emission over time.

Additionally, the color coordinates of the UCNPs were determined using the CIE 1931 color space diagram (Fig. 5d). These coordinates gradually transition from green to yellow-green as the synthesis time increases. At 20 min, the UCNPs emission closely matches green (approximately 540 nm), confirming the presence of green-emitting energy levels ( $^2H_{11/2}$  and  $^4S_{3/2}$ ) and optimal energy transfer between  $Yb^{3+}$  and  $Er^{3+}$ . At 25 min, the coordinates shift slightly toward yellow, confirming a higher population level of red ( $^4F_{9/2}$ ). This increase results from a more developed crystal structure due to extended synthesis time, which enhances overall crystal growth and modifies the environment surrounding the  $Er^{3+}$  ions. At 30 min,





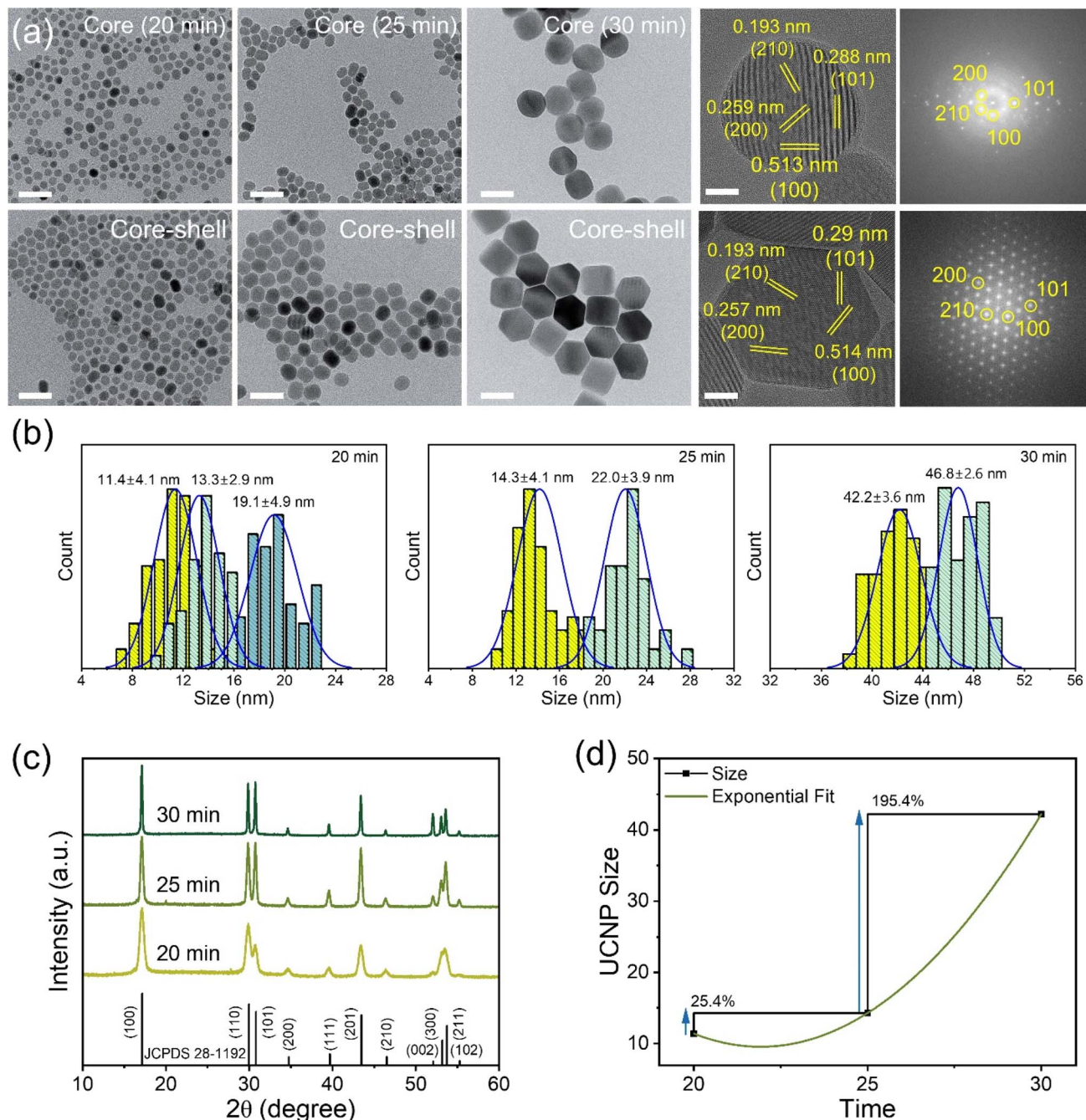


Fig. 4 (a) TEM images of the core synthesized for various durations (20 min, 25 min, and 30 min) alongside their core-shell UCNP. Scale bar = 50 nm. HR-TEM images and SAED patterns of core and core-shell UCNP synthesized with a growth time of 30 min. Scale bars in HR-TEM images = 5 nm. (b) Histograms of size distribution. (c) XRD patterns (10–60°) of core-shell UCNP. (d) Size of UCNP as a function of reaction time.

the color coordinates shift toward a more yellowish region as the synthesis time extends. This indicates a higher population of red ( $^4F_{9/2}$ ) levels compared to the green-emitting levels ( $^2H_{11/2}$  and  $^4S_{3/2}$ ), attributed to increased particle size and improved crystallinity from shell thickening, which reduces non-radiative green relaxation while favoring red emissions. These observations demonstrate that synthesis time significantly impacts UCNP color output. Time-controlled tuning of emissions is vital for applications requiring specific wavelengths, such as color

displays and multi-modal imaging, where distinct emissions enhance functionality and contrast.

The power dependence of luminescence intensities for Yb/Er-doped NaYF<sub>4</sub> UCNP synthesized under varying times was investigated. A slope near 1 indicates a linear relationship associated with single-photon processes,<sup>5,39,50</sup> while values approaching 2 correspond to two-photon processes.<sup>45</sup>

In Fig. 5e, over synthesis times of 20 min, 25 min, and 30 min, green emission slopes shifted toward higher-order

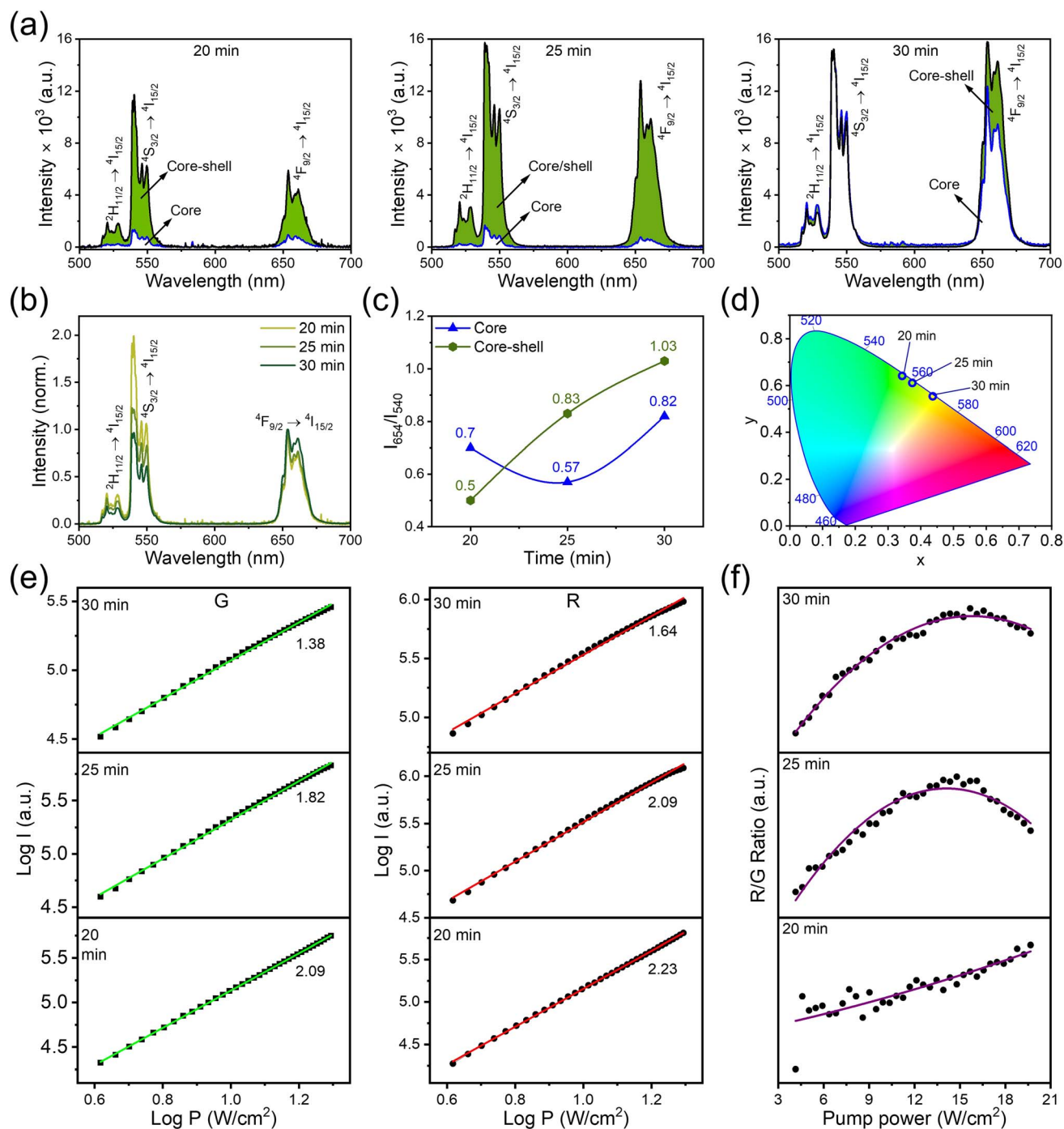


**Fig. 5** (a) Upconversion emission spectra of core and core-shell UCNP synthesized for 20 min, 25 min, and 30 min, all recorded under 980 nm laser excitation. (b) Normalized emission spectra at 654 nm. (c) Comparison of the red-to-green ( $I_{654}/I_{540}$ ) emission intensity as a function of time. (d) CIE chromaticity diagram for different growth durations: 20 min, 25 min, and 30 min. (e) Log  $I$  versus Log  $P$  for green and red emissions in core-shell UCNP, compared with excitation power density ( $P$ ). (f) R/G ratio versus pump power.

processes, particularly with the maximum slope of 2.09 at 20 min, decreasing with time up to 1.38 at 30 min. This variation reflects changes in particle size and crystal field environment affecting the energy transfer dynamics. A slope of 2.09, slightly above 2, confirms an efficient two-photon process with minimal multi-photon interactions. A slope of 1.82, close to 2, indicates a two-photon absorption process, while a sub-linear

slope of 1.38 suggests a complex upconversion mechanism involving multiple energy transfer steps between  $\text{Yb}^{3+}$  and  $\text{Er}^{3+}$  ions.<sup>12,51</sup> The red emission followed a similar trend, with consistently higher slopes than green emission across all conditions, ranging from 1.86 to 2.23 and decreasing from 2.23 to 1.64 as growth time extended from 20 min to 30 min. As growth time increased from 20 min to 30 min, power





dependence slopes decreased for both emissions, indicating reduced multi-photon upconversion efficiency. Shorter growth times produced smaller UCNPs with higher surface-to-volume ratios, affecting surface passivation and quenching effects.<sup>35</sup> For green emission, sub-linear slopes (<2) at 30 min confirm complex energy transfer dynamics within the core-shell structure.

The R/G ratio plot (Fig. 5f) indicates that increasing the reaction time from 20 min to 30 min significantly influences the optical properties of core-shell UCNPs, mainly reflected by the enhancement of the red-to-green emission (R/G) ratio. At shorter reaction times (20 min), the relatively low and gradually increasing R/G ratio with pump power suggests incomplete shell formation or less-developed crystallinity, leading to prominent non-radiative recombination processes and limited cross-relaxation efficiency towards red emission.<sup>10,13,35,39</sup> At the intermediate synthesis time (25 min), the nanoparticles exhibit improved crystallinity and effective core-shell interfaces, resulting in enhanced energy transfer and a noticeable saturation peak at higher pump powers. This saturation behavior indicates that at elevated excitation powers, the energy transfer pathway toward red emission becomes increasingly dominant until it reaches an equilibrium or saturation limit due to competitive energy-transfer processes.<sup>8,45</sup> Finally, extending the reaction time to 30 min yields a significantly higher maximum R/G ratio, suggesting optimal crystallization, reduced surface defects, and an effectively passivated core-shell interface, all contributing to highly efficient energy migration and cross-relaxation pathways favoring red emission.<sup>7,42</sup> The saturation at higher pump powers in the 30 min sample strongly supports the conclusion that optimized reaction conditions can improve upconversion emission characteristics, enabling fine-tuned optical properties for advanced bioimaging and photonic applications.

The observed evolution of nanoparticle size, morphological transitions, and luminescence characteristics in this study can be effectively explained by established nanoparticle growth mechanisms, particularly the La Mer model combined with Ostwald ripening.<sup>33</sup> Initially, nanoparticles nucleate rapidly when precursor concentrations exceed a critical supersaturation threshold, consistent with classical La Mer nucleation theory. These nucleation events produce small cubic phase nanoparticles that subsequently grow and undergo a thermodynamically favored transformation into hexagonal  $\beta$ -phase nanoparticles upon reaching a critical size. Further nanoparticle growth, especially at prolonged reaction times, primarily occurs *via* Ostwald ripening, in which smaller nanoparticles preferentially dissolve, releasing ions that subsequently redeposit onto larger nanoparticles. This mechanism significantly increases particle size and enhances crystallinity, aligning well with the kinetic studies by May *et al.* and Radunz *et al.*, which reported similar nucleation, phase transition, and ripening dynamics in NaYF<sub>4</sub>-based systems.<sup>33,36</sup> Additionally, observed variations in the red-to-green (R/G) emission ratio and nonlinear pump-power-dependent luminescence behavior can be attributed to size-dependent surface quenching and internal energy-transfer dynamics. Specifically, smaller nanoparticles

exhibit pronounced surface quenching, selectively enhancing the relative red emission intensity compared to green emission.<sup>4,46,52,53</sup> Conversely, core-shell architectures and optimized doping significantly reduce surface defects, improving luminescence efficiency. Collectively, these insights underscore the importance of precisely controlling synthesis parameters, particularly temperature and reaction duration, for tailoring UCNP properties in targeted bioimaging, sensing, and advanced photonic applications.

### 3 Conclusion

This study demonstrates a precise, systematic approach to synthesizing high-quality Yb<sup>3+</sup>/Er<sup>3+</sup>-doped NaYF<sub>4</sub> core-shell UCNPs by carefully tuning the reaction temperature and synthesis time. In summary, a growth temperature of 320 °C is optimal for synthesizing sub-10 nm core-shell UCNPs while preserving their optical properties. Additionally, small-sized (11.4 nm) UCNPs and highly crystalline larger UCNPs were successfully synthesized using our optimized methodology. Furthermore, reaction times about 50% shorter than conventional methods reduced nanoparticle aggregation and surface quenching effects, enabling precise control of particle size, morphology, and emission characteristics. Power-dependent emission analyses provided valuable insights into the efficient two-photon energy transfer mechanisms governing upconversion luminescence. The ability to reproducibly synthesize high-quality, ultrasmall UCNPs with controlled emission characteristics holds great promise for their integration into advanced biomedical imaging, nanoscale sensing, and photonic devices. Future investigations into surface engineering and further size reduction could expand their applicability, particularly in scenarios demanding minimal nanoparticle dimensions and high luminescence efficiency. These findings highlight the important role of reaction duration in nanoparticle engineering, illustrating that controlled synthesis time is crucial for tailoring UCNPs for specific bioimaging or photonic applications that require precise particle sizes and adjustable emission characteristics.

### Data availability

The data supporting this article have been included as part of the ESI†. Detailed experimental method and characterization data are provided therein.

### Author contributions

Umme Farva contributed to the conceptualization, methodology development, data curation, formal analysis, and writing of the original draft. Young Gwon Jung assisted with data curation and formal analysis. Kang Taek Lee was responsible for project administration, funding acquisition, supervision, resources, validation, and writing – review and editing. All authors have reviewed and approved the final version of the manuscript.



## Conflicts of interest

The authors declare no competing interest.

## Acknowledgements

This work was supported by the National Research Foundation of Korea (NRF) grant funded by the Korea government (MSIT) (RS-2024-00411137). Cs-TEM, TEM and XRD analyses were performed at the GIST Advanced Institute of Instrumental Analysis (GAIA) Gwangju, Republic of Korea.

## References

- 1 C. Liu, H. Wang, X. Li and D. Chen, Monodisperse, size-tunable and highly efficient  $\beta$ -NaYF<sub>4</sub>:Yb,Er(Tm) up-conversion luminescent nanospheres: controllable synthesis and their surface modifications, *J. Mater. Chem.*, 2009, **19**(21), 3546–3553, DOI: [10.1039/b820254k](#).
- 2 H. Schäfer, P. Ptacek, H. Eickmeier and M. Haase, Synthesis of Hexagonal Yb<sup>3+</sup>,Er<sup>3+</sup>-Doped NaYF<sub>4</sub> Nanocrystals at Low Temperature, *Adv. Funct. Mater.*, 2009, **19**(19), 3091–3097, DOI: [10.1002/adfm.200900642](#).
- 3 D. Li, Q. Shao, Y. Dong and J. Jiang, Phase-, shape- and size-controlled synthesis of NaYF<sub>4</sub>:Yb<sup>3+</sup>,Er<sup>3+</sup> nanoparticles using rare-earth acetate precursors, *J. Rare Earths*, 2014, **32**(11), 1032–1036, DOI: [10.1016/s1002-0721\(14\)60179-4](#).
- 4 S. Wilhelm, M. Kaiser, C. Wurth, J. Heiland, C. Carrillo-Carrion, V. Muhr, O. S. Wolfbeis, W. J. Parak, U. Resch-Genger and T. Hirsch, Water dispersible upconverting nanoparticles: effects of surface modification on their luminescence and colloidal stability, *Nanoscale*, 2015, **7**(4), 1403–1410, DOI: [10.1039/c4nr05954a](#).
- 5 C. Homann, L. Krukewitt, F. Frenzel, B. Grauel, C. Wurth, U. Resch-Genger and M. Haase, NaYF<sub>4</sub>:Yb,Er/NaYF<sub>4</sub> Core/Shell Nanocrystals with High Upconversion Luminescence Quantum Yield, *Angew Chem. Int. Ed. Engl.*, 2018, **57**(28), 8765–8769, DOI: [10.1002/anie.201803083](#).
- 6 J. Dolai, R. Ray, S. Ghosh, A. Maity and N. R. Jana, Optical Nanomaterials for Advanced Bioimaging Applications, *ACS Appl. Opt. Mater.*, 2023, **2**(1), 1–14, DOI: [10.1021/acsao.3c00357](#).
- 7 F. Li, L. Tu, Y. Zhang, D. Huang, X. Liu, X. Zhang, J. Du, R. Fan, C. Yang, K. W. Krämer, J. Marques-Hueso and G. Chen, Size-dependent lanthanide energy transfer amplifies upconversion luminescence quantum yields, *Nat. Photonics*, 2024, **18**, 440–449, DOI: [10.1038/s41566-024-01393-3](#).
- 8 S. Wen, J. Zhou, K. Zheng, A. Bednarkiewicz, X. Liu and D. Jin, Advances in highly doped upconversion nanoparticles, *Nat. Commun.*, 2018, **9**(1), 2415, DOI: [10.1038/s41467-018-04813-5](#).
- 9 B. Zheng, J. Fan, B. Chen, X. Qin, J. Wang, F. Wang, R. Deng and X. Liu, Rare-Earth Doping in Nanostructured Inorganic Materials, *Chem. Rev.*, 2022, **122**(6), 5519–5603, DOI: [10.1021/acs.chemrev.1c00644](#).
- 10 H. Dong, S. R. Du, X. Y. Zheng, G. M. Lyu, L. D. Sun, L. D. Li, P. Z. Zhang, C. Zhang and C. H. Yan, Lanthanide Nanoparticles: From Design toward Bioimaging and Therapy, *Chem. Rev.*, 2015, **115**(19), 10725–10815, DOI: [10.1021/acs.chemrev.5b00091](#).
- 11 X. Song, S. Li, H. Guo, W. You, X. Shang, R. Li, D. Tu, W. Zheng, Z. Chen, H. Yang and X. Chen, Graphene-Oxide-Modified Lanthanide Nanoprobes for Tumor-Targeted Visible/NIR-II Luminescence Imaging, *Angew Chem. Int. Ed. Engl.*, 2019, **58**(52), 18981–18986, DOI: [10.1002/anie.201909416](#).
- 12 Y. Xie, Y. Song, G. Sun, P. Hu, A. Bednarkiewicz and L. Sun, Lanthanide-doped heterostructured nanocomposites toward advanced optical anti-counterfeiting and information storage, *Light:Sci. Appl.*, 2022, **11**(1), 150, DOI: [10.1038/s41377-022-00813-9](#).
- 13 A. Fernandez-Bravo, K. Yao, E. S. Barnard, N. J. Borys, E. S. Levy, B. Tian, C. A. Tajon, L. Moretti, M. V. Altos, S. Aloni, K. Beketayev, F. Scotognella, B. E. Cohen, E. M. Chan and P. J. Schuck, Continuous-wave upconverting nanoparticle microlasers, *Nat. Nanotechnol.*, 2018, **13**(7), 572–577, DOI: [10.1038/s41565-018-0161-8](#).
- 14 S. Abbasi-Moayed, A. Bigdeli and M. R. Hormozi-Nezhad, Application of NaYF<sub>4</sub>:Yb/Er/Tm UCNPs in Array-Based Sensing of Neurotransmitters: From a Single Particle to a Multichannel Sensor Array, *ACS Appl. Mater. Interfaces*, 2020, **12**(47), 52976–52982, DOI: [10.1021/acsami.0c17200](#).
- 15 F. Xu, Y. Sun, H. Gao, S. Jin, Z. Zhang, H. Zhang, G. Pan, M. Kang, X. Ma and Y. Mao, High-Performance Perovskite Solar Cells Based on NaCsWO<sub>3</sub>@NaYF<sub>4</sub>:Yb,Er Upconversion Nanoparticles, *ACS Appl. Mater. Interfaces*, 2021, **13**(2), 2674–2684, DOI: [10.1021/acsami.0c19475](#).
- 16 S. Han, W. Sung, T. Y. Kim, S. J. Yang, S. Kim, G. Lee, K. Cho and S. K. Hahn, Upconversion nanoparticles coated organic photovoltaics for near infrared light controlled drug delivery systems, *Nano Energy*, 2021, **81**, 105650, DOI: [10.1016/j.nanoen.2020.105650](#).
- 17 T. Zhang, H. Lin, L. Cui, N. An, R. Tong, Y. Chen, C. Yang, X. Li, J. Liu and F. Qu, Near Infrared Light Triggered Reactive Oxygen Species Responsive Upconversion Nanoplatforrm for Drug Delivery and Photodynamic Therapy, *Eur. J. Inorg. Chem.*, 2016, **2016**(8), 1206–1213, DOI: [10.1002/ejic.201501320](#).
- 18 X. Zhang, W. Chen, X. Xie, Y. Li, D. Chen, Z. Chao, C. Liu, H. Ma, Y. Liu and H. Ju, Boosting Luminance Energy Transfer Efficiency in Upconversion Nanoparticles with an Energy-Concentrating Zone, *Angew Chem. Int. Ed. Engl.*, 2019, **58**(35), 12117–12122, DOI: [10.1002/anie.201906380](#).
- 19 A. Hlavacek, Z. Farka, M. J. Mickert, U. Kostiv, J. C. Brandmeier, D. Horak, P. Skladal, F. Foret and H. H. Gorris, Bioconjugates of photon-upconversion nanoparticles for cancer biomarker detection and imaging, *Nat. Protoc.*, 2022, **17**(4), 1028–1072, DOI: [10.1038/s41596-021-00670-7](#).
- 20 T. Rao, Y. Xu, X. Tang and G. Mu, Review of Photon-to-Photon Conversion in Nanoscale Materials and Devices



- and Its Applications, *ACS Appl. Nano Mater.*, 2023, 7(1), 904–918, DOI: [10.1021/acsnm.3c04950](https://doi.org/10.1021/acsnm.3c04950).
- 21 S. Zha, H. Liu, H. Li, H. Li, K. L. Wong and A. H. All, Functionalized Nanomaterials Capable of Crossing the Blood–Brain Barrier, *ACS Nano*, 2024, 18(3), 1820–1845, DOI: [10.1021/acsnano.3c10674](https://doi.org/10.1021/acsnano.3c10674).
  - 22 F. Wang, R. Deng and X. Liu, Preparation of core-shell NaGdF<sub>4</sub> nanoparticles doped with luminescent lanthanide ions to be used as upconversion-based probes, *Nat. Protoc.*, 2014, 9(7), 1634–1644, DOI: [10.1038/nprot.2014.111](https://doi.org/10.1038/nprot.2014.111).
  - 23 E. Andresen, F. Islam, C. Prinz, P. Gehrmann, K. Licha, J. Roik, S. Recknagel and U. Resch-Genger, Assessing the reproducibility and up-scaling of the synthesis of Er,Yb-doped NaYF<sub>4</sub>-based upconverting nanoparticles and control of size, morphology, and optical properties, *Sci. Rep.*, 2023, 13(1), 2288, DOI: [10.1038/s41598-023-28875-8](https://doi.org/10.1038/s41598-023-28875-8).
  - 24 Q. Wang, M. C. Tan, R. Zhuo, G. A. Kumar and R. E. Riman, A solvothermal route to size- and phase-controlled highly luminescent NaYF<sub>4</sub>:Yb,Er up-conversion nanocrystals, *J. Nanosci. Nanotechnol.*, 2010, 10(3), 1685–1692, DOI: [10.1166/jnn.2010.2120](https://doi.org/10.1166/jnn.2010.2120).
  - 25 T. Rinkel, J. Nordmann, A. N. Raj and M. Haase, Ostwald-ripening and particle size focussing of sub-10 nm NaYF<sub>4</sub> upconversion nanocrystals, *Nanoscale*, 2014, 6(23), 14523–14530, DOI: [10.1039/c4nr03833a](https://doi.org/10.1039/c4nr03833a).
  - 26 X. Zhai, Y. Wang, X. Liu, S. Liu, P. Lei, S. Yao, S. Song, L. Zhou, J. Feng and H. Zhang, A Simple Strategy for the Controlled Synthesis of Ultrasmall Hexagonal-Phase NaYF<sub>4</sub>:Yb,Er Upconversion Nanocrystals, *ChemPhotoChem*, 2017, 1(8), 369–375, DOI: [10.1002/cptc.201700013](https://doi.org/10.1002/cptc.201700013).
  - 27 A. D. Ostrowski, E. M. Chan, D. J. Gargas, E. M. Katz, G. Han, P. J. Schuck, D. J. Milliron and B. E. Cohen, Controlled Synthesis and Single-Particle Imaging of Bright, Sub-10 nm Lanthanide-Doped Upconverting Nanocrystals, *ACS Nano*, 2012, 6(3), 2686–2692, DOI: [10.1021/nn3000737](https://doi.org/10.1021/nn3000737).
  - 28 S. F. Himmelstoß and T. Hirsch, Long-Term Colloidal and Chemical Stability in Aqueous Media of NaYF<sub>4</sub>-Type Upconversion Nanoparticles Modified by Ligand-Exchange, *Part. Part. Syst. Charact.*, 2019, 36(10), 1900235, DOI: [10.1002/ppsc.201900235](https://doi.org/10.1002/ppsc.201900235).
  - 29 M. Quintanilla, E. Hemmer, J. Marques-Hueso, S. Rohani, G. Lucchini, M. Wang, R. R. Zamani, V. Roddatis, A. Speghini, B. S. Richards and F. Vetrone, Cubic versus hexagonal – phase, size and morphology effects on the photoluminescence quantum yield of NaGdF<sub>4</sub>:Er<sup>3+</sup>/Yb<sup>3+</sup> upconverting nanoparticles, *Nanoscale*, 2022, 14(4), 1492–1504, DOI: [10.1039/d1nr06319g](https://doi.org/10.1039/d1nr06319g).
  - 30 C. Würth, B. Grauel, M. Pons, F. Frenzel, P. Rissiek, K. Rücker, M. Haase and U. Resch-Genger, Yb- and Er concentration dependence of the upconversion luminescence of highly doped NaYF<sub>4</sub>:Yb,Er/NaYF<sub>4</sub>:Lu core/shell nanocrystals prepared by a water-free synthesis, *Nano Res.*, 2022, 15(10), 9639–9646, DOI: [10.1007/s12274-022-4570-5](https://doi.org/10.1007/s12274-022-4570-5).
  - 31 L. Schneider, T. Rinkel, B. Voss, A. Chrobak, J. P. Klare, J. Neethling, J. Olivier, D. Schaniel, E. Bendeif el, F. Bondino, *et al.*, Characterization of multifunctional beta-NaEuF<sub>4</sub>/NaGdF<sub>4</sub> core-shell nanoparticles with narrow size distribution, *Nanoscale*, 2016, 8(5), 2832–2843, DOI: [10.1039/c5nr06915g](https://doi.org/10.1039/c5nr06915g).
  - 32 T. Rinkel, A. N. Raj, S. Duhnen and M. Haase, Synthesis of 10 nm beta-NaYF<sub>4</sub>:Yb,Er/NaYF<sub>4</sub> Core/Shell Upconversion Nanocrystals with 5 nm Particle Cores, *Angew. Chem. Int. Ed. Engl.*, 2016, 55(3), 1164–1167, DOI: [10.1002/anie.201508838](https://doi.org/10.1002/anie.201508838).
  - 33 P. B. May, J. D. Suter, P. S. May and M. T. Berry, The Dynamics of Nanoparticle Growth and Phase Change During Synthesis of β-NaYF<sub>4</sub>, *J. Phys. Chem. C*, 2016, 120(17), 9482–9489, DOI: [10.1021/acs.jpcc.6b01365](https://doi.org/10.1021/acs.jpcc.6b01365).
  - 34 F. Zhang, R. Che, X. Li, C. Yao, J. Yang, D. Shen, P. Hu, W. Li and D. Zhao, Direct imaging the upconversion nanocrystal core/shell structure at the subnanometer level: shell thickness dependence in upconverting optical properties, *Nano Lett.*, 2012, 12(6), 2852–2858, DOI: [10.1021/nl300421n](https://doi.org/10.1021/nl300421n).
  - 35 F. T. Rabouw, P. T. Prins, P. Villanueva-Delgado, M. Castelijns, R. G. Geitenbeek and A. Meijerink, Quenching Pathways in NaYF<sub>4</sub>:Er<sup>3+</sup>,Yb<sup>3+</sup> Upconversion Nanocrystals, *ACS Nano*, 2018, 12(5), 4812–4823, DOI: [10.1021/acsnano.8b01545](https://doi.org/10.1021/acsnano.8b01545).
  - 36 S. Radunz, A. Schavkan, S. Wahl, C. Würth, H. R. Tschiche, M. Krumrey and U. Resch-Genger, Evolution of Size and Optical Properties of Upconverting Nanoparticles during High-Temperature Synthesis, *J. Phys. Chem. C*, 2018, 122(50), 28958–28967, DOI: [10.1021/acs.jpcc.8b09819](https://doi.org/10.1021/acs.jpcc.8b09819).
  - 37 Y. I. Park, J. H. Kim, K. T. Lee, K. S. Jeon, H. B. Na, J. H. Yu, H. M. Kim, N. Lee, S. H. Choi, S. I. Baik, *et al.*, Nonblinking and Nonbleaching Upconverting Nanoparticles as an Optical Imaging Nanoprobe and T1 Magnetic Resonance Imaging Contrast Agent, *Adv. Mater.*, 2009, 21(44), 4467–4471, DOI: [10.1002/adma.200901356](https://doi.org/10.1002/adma.200901356).
  - 38 K. Zhang, L. Yang, F. Lu, X. Wu and J. J. Zhu, A Universal Upconversion Sensing Platform for the Sensitive Detection of Tumour-Related ncRNA through an Exo III-Assisted Cycling Amplification Strategy, *Small*, 2018, 14(10), 1703858, DOI: [10.1002/smll.201703858](https://doi.org/10.1002/smll.201703858).
  - 39 L. T. K. Giang, K. Trejgis, L. Marciniak, N. Vu and L. Q. Minh, Fabrication and characterization of up-converting beta-NaYF<sub>4</sub>:Er<sup>3+</sup>,Yb<sup>3+</sup>@NaYF<sub>4</sub> core-shell nanoparticles for temperature sensing applications, *Sci. Rep.*, 2020, 10(1), 14672, DOI: [10.1038/s41598-020-71606-6](https://doi.org/10.1038/s41598-020-71606-6).
  - 40 T. van Westen and R. D. Groot, Effect of Temperature Cycling on Ostwald Ripening, *Cryst. Growth Des.*, 2018, 18(9), 4952–4962, DOI: [10.1021/acs.cgd.8b00267](https://doi.org/10.1021/acs.cgd.8b00267).
  - 41 L. Tu, K. Wu, Y. Luo, E. Wang, J. Yuan, J. Zuo, D. Zhou, B. Li, J. Zhou, D. Jin, *et al.*, Significant Enhancement of the Upconversion Emission in Highly Er<sup>3+</sup>-Doped Nanoparticles at Cryogenic Temperatures, *Angew. Chem. Int. Ed. Engl.*, 2023, 62(7), e202217100, DOI: [10.1002/anie.202217100](https://doi.org/10.1002/anie.202217100).
  - 42 Y. Zhang, R. Wen, J. Hu, D. Guan, X. Qiu, Y. Zhang, D. S. Kohane and Q. Liu, Enhancement of single upconversion nanoparticle imaging by topologically segregated core-shell structure with inward energy





- migration, *Nat. Commun.*, 2022, **13**(1), 5927, DOI: [10.1038/s41467-022-33660-8](#).
- 43 N. Bogdan, F. Vetrone, G. A. Ozin and J. A. Capobianco, Synthesis of ligand-free colloidally stable water dispersible brightly luminescent lanthanide-doped upconverting nanoparticles, *Nano Lett.*, 2011, **11**(2), 835–840, DOI: [10.1021/nl1041929](#).
- 44 Y. I. Park, H. M. Kim, J. H. Kim, K. C. Moon, B. Yoo, K. T. Lee, N. Lee, Y. Choi, W. Park, D. Ling, *et al.*, Theranostic probe based on lanthanide-doped nanoparticles for simultaneous *in vivo* dual-modal imaging and photodynamic therapy, *Adv. Mater.*, 2012, **24**(42), 5755–5761, DOI: [10.1002/adma.201202433](#).
- 45 T. Jung, H. L. Jo, S. H. Nam, B. Yoo, Y. Cho, J. Kim, H. M. Kim, T. Hyeon, Y. D. Suh, H. Lee and K. T. Lee, The preferred upconversion pathway for the red emission of lanthanide-doped upconverting nanoparticles,  $\text{NaYF}_4:\text{Yb}^{3+}, \text{Er}^{3+}$ , *Phys. Chem. Chem. Phys.*, 2015, **17**(20), 13201–13205, DOI: [10.1039/c5cp01634g](#).
- 46 M. Pollnau, D. R. Gamelin, S. R. Luthi and H. U. Gudel, Power dependence of upconversion luminescence in lanthanide and transition-metal-ion systems, *Phys. Rev. B:Condens. Matter Mater. Phys.*, 2000, **61**(5), 3337, DOI: [10.1103/PhysRevB.61.3337](#).
- 47 J. C. Boyer and F. C. van Veggel, Absolute quantum yield measurements of colloidal  $\text{NaYF}_4:\text{Er}^{3+}, \text{Yb}^{3+}$  upconverting nanoparticles, *Nanoscale*, 2010, **2**(8), 1417–1419, DOI: [10.1039/c0nr00253d](#).
- 48 A. F. García-Flores, E. D. Martínez, J. Munevar, D. J. Garcia, P. S. Cornaglia, F. Fabris, R. R. Urbano and C. Rettori, Crystal-field Stark effect on the upconversion light emission spectrum of  $\alpha\text{-NaYF}_4$  nanoparticles doped with  $\text{Dy}^{3+}$ ,  $\text{Er}^{3+}$ , or  $\text{Yb}^{3+}$ , *Phys. Rev. B*, 2022, **106**(12), 125427, DOI: [10.1103/PhysRevB.106.125427](#).
- 49 M. He, P. Huang, C. Zhang, J. Ma, R. He and D. Cui, Phase- and size-controllable synthesis of hexagonal upconversion rare-earth fluoride nanocrystals through an oleic acid/ionic liquid two-phase system, *Chemistry*, 2012, **18**(19), 5954–5969, DOI: [10.1002/chem.201102419](#).
- 50 O. Dukhno, S. Ghosh, V. Greiner, S. Bou, J. Godet, V. Muhr, M. Buchner, T. Hirsch, Y. Mely and F. Przybilla, Targeted Single Particle Tracking with Upconverting Nanoparticles, *ACS Appl. Mater. Interfaces*, 2024, **16**(9), 11217–11227, DOI: [10.1021/acsami.3c17116](#).
- 51 F. S. J. K. Ma, H. W. Toll, O. Salinas, X. Ma and C. S. Peng, Multicolor Long-Term Single-Particle Tracking Using 10 nm Upconverting Nanoparticles, *Nano Lett.*, 2024, **24**(14), 4194–4201, DOI: [10.1021/acs.nanolett.4c00207](#).
- 52 Q. Liu, Y. Zhang, C. S. Peng, T. Yang, L. M. Joubert and S. Chu, Single upconversion nanoparticle imaging at sub-10 W cm<sup>-2</sup> irradiance, *Nat. Photonics*, 2018, **12**(9), 548–553, DOI: [10.1038/s41566-018-0217-1](#).
- 53 X. Liu, L. Tu, F. Li, D. Huang, H. Agren and G. Chen, Unravelling Size-Dependent Upconversion Luminescence in Ytterbium and Erbium Codoped  $\text{NaYF}_4$  Nanocrystals, *J. Am. Chem. Soc.*, 2025, **147**(7), 5955–5961, DOI: [10.1021/jacs.4c15683](#).

